Measurement of the ^{14}N(n, p) ^{14}C cross section at the CERN n_TOF facility from subthermal energy to 800 keV

Pablo Torres-Sánchez,[1,*] Javier Praena,[1] Ignacio Porras,[1] Marta Sabaté-Gilarte,[2,3] Claudia Lederer-Woods,[4] Oliver Aberle,[2] Victor Alcayne,[5] Simone Amaducci,[6,7] Józef Andrzejewski,[8] Laurent Audouin,[9] Vicente Bécares,[5] Victor Babiano-Suarez,[10] Michael Bacak,[2,11,12] Massimo Barbagallo,[2,13] František Bečvář,[14] Giorgio Bellia,[6,7] Eric Berthoumieux,[12] Jon Billowes,[15] Damir Bosnar,[16] Adam Brown,[17] Maurizio Busso,[18,19] Manuel Caamaño,[20] Luis Caballero,[10] Francisco Calviño,[21] Marco Calviani,[2] Daniel Cano-Ott,[5] Adria Casanovas,[21] Francesco Cerutti,[2] Yonghao Chen,[9] Enrico Chiaveri,[2,15,3] Nicola Colonna,[13] Guillem Cortés,[21] Miguel Cortés-Giraldo,[3] Luigi Cosentino,[6] Sergio Cristallo,[18,22] Lucia-Anna Damone,[13,23] Maria Diakaki,[24,2] Mirco Dietz,[4] César Domingo-Pardo,[10] Rugard Dressler,[25] Emmeric Dupont,[12] Ignacio Durán,[20] Zinovia Eleme,[26] Beatriz Fernández-Domínguez,[20] Alfredo Ferrari,[2] Francisco Javier Ferrer,[27,3] Paolo Finocchiaro,[6] Valter Furman,[28] Kathrin Göbel,[29] Ruchi Garg,[4] Aleksandra Gawlik-Ramięga,[8] Benoit Geslot,[30] Simone Gilardoni,[2] Tudor Glodariu,[31,†] Isabel Gonçalves,[32] Enrique González-Romero,[5] Carlos Guerrero,[3] Frank Gunsing,[12] Hideo Harada,[33] Stephan Heinitz,[25] Jan Heyse,[34] David Jenkins,[17] Erwin Jericha,[11] Franz Käppeler,[35,†] Yacine Kadi,[2] Atsushi Kimura,[33] Niko Kivel,[25] Michael Kokkoris,[24] Yury Kopatch,[28] Milan Krtička,[14] Deniz Kurtulgil,[29] Ion Ladarescu,[10] Helmut Leeb,[11] Jorge Lerendegui-Marco,[3] Sergio Lo Meo,[36,37] Sarah-Jane Lonsdale,[4] Daniela Macina,[2] Alice Manna,[37,38] Trinitario Martínez,[5] Alessandro Masi,[2] Cristian Massimi,[37,38] Pierfrancesco Mastinu,[39] Mario Mastromarco,[2] Francesca Matteucci,[40,41] Emilio-Andrea Maugeri,[25] Annamaria Mazzone,[13,42] Emilio Mendoza,[5] Alberto Mengoni,[36] Veatriki Michalopoulou,[24] Paolo Maria Milazzo,[40] Federica Mingrone,[2] Agatino Musumarra,[6,7] Alexandru Negret,[31] Ralf Nolte,[43] Francisco Ogállar,[1] Andreea Oprea,[31] Nikolas Patronis,[26] Andreas Pavlik,[44] Jarosław Perkowski,[8] Luciano Persanti,[13,18,22] José-Manuel Quesada,[3] Désirée Radeck,[43] Diego Ramos-Doval,[9] Thomas Rauscher,[45,46] René Reifarth,[29] Dimitri Rochman,[25] Carlo Rubbia,[2] Alok Saxena,[47] Peter Schillebeeckx,[34] Dorothea Schumann,[25] Gavin Smith,[15] Nikolay Sosnin,[15] Athanasios Stamatopoulos,[24] Giuseppe Tagliente,[13] José Tain,[10] Zeynep Talip,[25] Ariel Tarifeño-Saldivia,[21] Laurent Tassan-Got,[2,24,9] Andrea Tsinganis,[2] Jiri Ulrich,[25] Sebastian Urlass,[2,48] Stanislav Valenta,[14] Gianni Vannini,[37,38] Vincenzo Variale,[13] Pedro Vaz,[32] Alberto Ventura,[37] Vasilis Vlachoudis,[2] Rosa Vlastou,[24] Anton Wallner,[49] PhilipJohn Woods,[4] Tobias Wright,[15] and Petar Žugec[16]

(The n_TOF Collaboration)[‡]

[1]*University of Granada, Granada, Spain*
[2]*European Organization for Nuclear Research (CERN), Geneva, Switzerland*
[3]*Universidad de Sevilla, Seville, Spain*
[4]*School of Physics and Astronomy, University of Edinburgh, Edinburgh, United Kingdom*
[5]*Centro de Investigaciones Energéticas Medioambientales y Tecnológicas (CIEMAT), Madrid, Spain*
[6]*INFN Laboratori Nazionali del Sud, Catania, Italy*
[7]*Dipartimento di Fisica e Astronomia, Università di Catania, Catania, Italy*
[8]*University of Lodz, Lodz, Poland*
[9]*Institut de Physique Nucléaire, CNRS-IN2P3, Université Paris-Sud, Université Paris-Saclay, F-91406 Orsay Cedex, France*
[10]*Instituto de Física Corpuscular, CSIC - Universidad de Valencia, Valencia, Spain*
[11]*TU Wien, Atominstitut, Stadionallee 2, 1020 Wien, Austria*
[12]*CEA Irfu, Université Paris-Saclay, F-91191 Gif-sur-Yvette, France*
[13]*Istituto Nazionale di Fisica Nucleare, Sezione di Bari, Bari, Italy*
[14]*Charles University, Prague, Czech Republic*
[15]*University of Manchester, Manchester, United Kingdom*
[16]*Department of Physics, Faculty of Science, University of Zagreb, Zagreb, Croatia*
[17]*University of York, York, United Kingdom*
[18]*Istituto Nazionale di Fisica Nucleare, Sezione di Perugia, Perugia, Italy*
[19]*Dipartimento di Fisica e Geologia, Università di Perugia, Perugia, Italy*
[20]*University of Santiago de Compostela, Santiago de Compostela, Spain*
[21]*Universitat Politècnica de Catalunya, Barcelona, Spain*
[22]*Istituto Nazionale di Astrofisica - Osservatorio Astronomico di Teramo, Teramo, Italy*
[23]*Dipartimento Interateneo di Fisica, Università degli Studi di Bari, Bari, Italy*

[*]pablotorres@ugr.es
[†]Deceased.
[‡]www.cern.ch/ntof

[24]*National Technical University of Athens, Athens, Greece*
[25]*Paul Scherrer Institut (PSI), Villigen, Switzerland*
[26]*University of Ioannina, Ioannina, Greece*
[27]*Centro Nacional de Aceleradores (CNA), Seville, Spain*
[28]*Joint Institute for Nuclear Research (JINR), Dubna, Russia*
[29]*Goethe University Frankfurt, Frankfurt-am-Main, Germany*
[30]*CEA Cadarache, DES, Saint-Paul-les-Durance 13108, France*
[31]*Horia Hulubei National Institute of Physics and Nuclear Engineering, Bucharest-Magurele, Romania*
[32]*Instituto Superior Técnico, Lisbon, Portugal*
[33]*Japan Atomic Energy Agency (JAEA), Tokai-Mura, Japan*
[34]*Joint Research Centre (JRC), European Commission, Geel, Belgium*
[35]*Karlsruhe Institute of Technology, Campus North, IKP, 76021 Karlsruhe, Germany*
[36]*Agenzia Nazionale per le Nuove Tecnologie (ENEA), Bologna, Italy*
[37]*Istituto Nazionale di Fisica Nucleare, Sezione di Bologna, Bologna, Italy*
[38]*Dipartimento di Fisica e Astronomia, Università di Bologna, Bologna, Italy*
[39]*Istituto Nazionale di Fisica Nucleare, Sezione di Legnaro, Italy*
[40]*Istituto Nazionale di Fisica Nucleare, Sezione di Trieste, Trieste, Italy*
[41]*Dipartimento di Astronomia, Università di Trieste, Trieste, Italy*
[42]*Consiglio Nazionale delle Ricerche, Bari, Italy*
[43]*Physikalisch-Technische Bundesanstalt (PTB), Bundesallee 100, 38116 Braunschweig, Germany*
[44]*Faculty of Physics, University of Vienna, Vienna, Austria*
[45]*Department of Physics, University of Basel, Basel, Switzerland*
[46]*Centre for Astrophysics Research, University of Hertfordshire, Hatfield, United Kingdom*
[47]*Bhabha Atomic Research Centre (BARC), Mumbai, India*
[48]*Helmholtz-Zentrum Dresden-Rossendorf, Dresden, Germany*
[49]*Australian National University, Canberra, Australia*

(Received 15 December 2022; accepted 22 May 2023; published 29 June 2023)

Background: The ^{14}N(n, p) ^{14}C reaction is of interest in neutron capture therapy, where nitrogen-related dose is the main component due to low-energy neutrons, and in astrophysics, where ^{14}N acts as a neutron poison in the *s* process. Several discrepancies remain between the existing data obtained in partial energy ranges: thermal energy, keV region, and resonance region.
Purpose: We aim to measure the ^{14}N(n, p) ^{14}C cross section from thermal to the resonance region in a single measurement for the first time, including characterization of the first resonances, and provide calculations of Maxwellian averaged cross sections (MACS).
Method: We apply the time-of-flight technique at Experimental Area 2 (EAR-2) of the neutron time-of-flight (n_TOF) facility at CERN. ^{10}B(n, α) ^{7}Li and ^{235}U(n, f) reactions are used as references. Two detection systems are run simultaneously, one on beam and another off beam. Resonances are described with the *R*-matrix code SAMMY.
Results: The cross section was measured from subthermal energy to 800 keV, resolving the first two resonances (at 492.7 and 644 keV). A thermal cross section was obtained (1.809 ± 0.045 b) that is lower than the two most recent measurements by slightly more than one standard deviation, but in line with the ENDF/B-VIII.0 and JEFF-3.3 evaluations. A $1/v$ energy dependence of the cross section was confirmed up to tens of keV neutron energy. The low energy tail of the first resonance at 492.7 keV is lower than suggested by evaluated values, while the overall resonance strength agrees with evaluations.
Conclusions: Our measurement has allowed determination of the ^{14}N(n, p) cross section over a wide energy range for the first time. We have obtained cross sections with high accuracy (2.5%) from subthermal energy to 800 keV and used these data to calculate the MACS for $kT = 5$ to $kT = 100$ keV.

DOI: 10.1103/PhysRevC.107.064617

I. INTRODUCTION

The ^{14}N(n, p) ^{14}C reaction plays a key role in many fields. It is relevant in nuclear astrophysics because it is a significant neutron poison in the *s*-process nucleosynthesis [1]. Also, this reaction is an important proton feeder in the production of fluorine, via the chain of reactions ^{18}O(p, α) ^{15}N(α, γ) ^{19}F. ^{19}F is a useful tracer of the physical conditions in stellar interiors, since it can be easily destroyed by proton or α reactions, hence any production site needs also to enable ^{19}F to escape from the stellar interiors as it is observed with high abundance in asymptotic giant branch (AGB) star atmospheres [2]. In radiotherapy, the dose in healthy tissues is a limiting factor. Specifically, in boron neutron capture therapy (BNCT), the

^{14}N(n, p) ^{14}C reaction constitutes the main contribution to the dose in healthy tissue due to thermal neutrons [3], therefore it is crucial for determining the delivered dose in a BNCT treatment [4]. In addition, the International Commission on Radiation Units and Measurements (ICRU) recommends that the delivered dose should have less than 5% deviation from the prescribed dose [5]. At present, nuclear data are under review and upgrade for the new IAEA Technical Document (TECDOC) on BNCT [6]. An accurate ^{14}N(n, p) ^{14}C cross section is one of most important data to be considered there.

The ^{14}N(n, p) ^{14}C reaction has been measured several times, though all of these measurements have been focused on a specific energy region: thermal energy (25.3 meV), $1/v$ region (up to a few tens of keV), integral measurements in the keV range (25–200 keV), or resonance region (above 400 keV). Thus, there is no single measurement connecting the thermal energy or the $1/v$ region with the resonance region. The first resonance is above 450 keV. Despite the number of experiments, there are some issues that need to be clarified in the different energy ranges.

At thermal energy, there are several measurements [7–13] with values from 1.7 to 2.0 b. The last two provided 1.93 ± 0.05 b [12] and 1.868 ± 0.006 b [13], and they are higher than the ENDF/B-VIII.0 and JEFF-3.3 evaluations (1.8271 b) [14]. In BNCT, the disparities between measurements and evaluations in involved reactions can lead to differences up to 15% in the thermal neutron dose estimation in human tissues and 3–4% in total dose in no-tumor tissues (including γ and boron-induced doses). Thus, a reduction of the uncertainty in the ^{14}N(n, p) reaction leads to more accurate treatments, approaching ICRU recommendations [5]. The thermal value is also relevant in astrophysics. For instance, it has been shown that the thermal value impacts considerably the Maxwellian averaged cross section (MACS) for (n, p) reactions [15].

The only differential measurement available in the $1/v$ region is by Koehler *et al.* [16], covering the range from 61 meV to 35 keV. It was normalized by extrapolation to the thermal value in the Nuclear Data Compilation by Ajzenberg-Selove, at 1.83 ± 0.03 b [17]. In a second measurement, Koehler *et al.* confirmed the assumed value at thermal energy [18], obtaining the same results as Gledenov *et al.* [11]. Between 35 and 150 keV, there are no differential measurements, and there are only derived data from the inverse-reaction measurement by Gibbons *et al.* [19].

In the astrophysical range several integral measurements have been carried out [1,20–23]. For all of them there is a good agreement at 25 keV, except for those by Brehm *et al.* [20]. However, some differences arise in the measurements above 25 keV. Shima *et al.* [23] observed a reduction in the cross sections from 1.67 mb at 35.8 keV to 1.19 mb at 67.1 keV, while Gledenov *et al.* [21] saw a mostly flat behavior between 24.5 and 144 keV with values oscillating between 2.04 and 2.08 mb. The last measurement by Wallner *et al.* [1] encountered a reduction above 25 keV, with values of 0.88 and 0.90 mb at 123 and 178 keV, respectively, in clear disagreement with Gledenov *et al.* [21].

In the resonance region the most important measurements were carried out by Johnson *et al.* [24] and Morgan [25]. Johnson *et al.* measured the cross section from 150 keV to 2.15 MeV, using neutrons from a lithium target bombarded by protons with an energy spread of 5 keV [24]. Later, Morgan [25] using time of flight measured above 450 keV with better resolution, although he did not provide an analysis of the resonance parameters. Morgan is the reference for the evaluations in the resonance region. More recently, based on the comparison of the aforementioned cross section determined at 123 and 178 keV (at the low-energy tail of the first resonance at 492.7 keV) with the ENDF data in this region, Wallner *et al.* suggested a factor of about 3.3 lower strength for this resonance.

The ENDF/B-VIII.0 evaluation does not provide resonance parameters for this reaction, and refers to the compilation by Ajzenberg-Selove [17]. Information on the resonance parameters could be also obtained via other reactions that lead to the same compound nucleus [26]. Specifically, the inverse ^{14}C(p, n) ^{14}N reaction, whose threshold allows the observation of the lowest neutron resonances, has been used to provide information on their J^π [19,27–29]. Other reactions have thresholds above these states of ^{15}N [17]. Some measurements found an anisotropy in the first resonance [28] (indicating $J > \frac{1}{2}$), while others did not [19]. The neutron polarization measurement by Niecke *et al.* [29] reported a positive parity for this state. Contrarily, negative parity was assigned in another measurement [27] and in other compilations [17,30].

To summarize, although the ^{14}N(n, p) ^{14}C cross-section has been measured several times in different energy ranges, many open questions remain. In order to solve the discrepancies found in the ^{14}N(n, p) ^{14}C reaction, a measurement covering the range from thermal neutron energy to the first two resonances was carried out at the Experimental Area 2 of the n_TOF facility at CERN. The neutron beam at this experimental area presents an excellent compromise between high neutron flux, in particular at thermal energy, and energy resolution. The present measurement has covered by far the largest neutron energy range, and, in particular, for the first time has connected the thermal, $1/v$, and resonance regions. This has allowed an accurate analysis of the resonances, providing new information on the cross section in different energy ranges. This measurement is a part of the scientific program of the n_TOF Collaboration, including a series of experiments aiming at studying reactions of relevant interest in nuclear astrophysics and in medical physics [31].

II. EXPERIMENTAL SETUP

A. The n_TOF neutron beam

The experiment was performed at the Experimental Area 2 (EAR-2) of the n_TOF facility at CERN, located around 19.5 m from the neutron production target in the vertical direction. The neutrons are generated by the 20 GeV/c proton beam from the CERN Proton Synchrotron (PS) impinging onto a lead target. The technical features of the facility and the characteristics of the neutron beam are described in detail in Refs. [32,33].

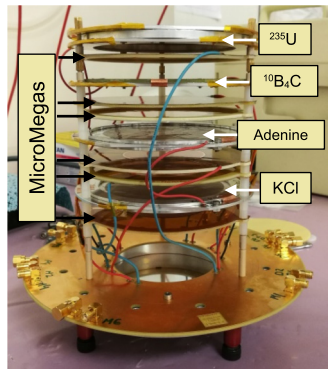

FIG. 1. The MicroMegas setup, with the six targets and six MicroMegas detectors used in the measurement. Adenine and KCl samples were placed in back-to-back pairs.

B. Detectors and data acquisition

The experimental setup for charged particle detection consisted of a couple of separate systems that worked in parallel. The first of them (upstream) was based on a stack of micromesh gaseous structure detectors (MicroMegas), while the second (downstream) used double-sided silicon strip detectors (DSSSD). The MicroMegas detectors are based on microbulk technology, for which the low mass, robustness, and neutron and γ transparency allow the use of several detectors along the beam with minimal perturbation. This allows a geometrical efficiency close to 50% when one of the two reaction products is detected [34]. This type of detector has been used thoroughly in n_TOF fission and charged-particle emission measurements, including the neutron flux determination [33,35]. A stack of MicroMegas detectors (9.5 cm in diameter) was mounted in a common reaction chamber as shown in Fig. 1, and operated with a gas mixture of 90% Ar and 10% CF_4. The beam-spot size at the position of the first sample was 1.91 cm (FWHM). The ^{235}U and ^{10}B samples were placed in the forward direction, the two nitrogen (adenine) samples were placed in a back-to-back configuration, and two KCl samples, which were used for a separate measurement (not analyzed in this work), were placed in the same configuration as the adenine samples. Additional measurements, replacing the adenine samples with dummy samples (Al foils as in the substrate of the adenine samples), were carried out in order to determine the background and reduce systematic uncertainties.

The DSSSD are silicon detectors that provide position sensitivity and allow background subtraction by means of front-rear strip coincidence analysis. W1 Model DC Strip Detectors with 16 × 16 strips from Micron Semiconductors (Design W D/S Type 2M/2M. Rrg No A-4366 and Ceramic substrate Number A-4331) were used [36]. These detectors have to be placed off-beam where a lower beam-related background is found, at the cost of a lower geometrical efficiency. The DSSSD allow one to extend the measured neutron energy range toward high energy and also analyze the angular distribution of the emitted protons. The setup, shown in Fig. 2, consisted of a couple of detectors, one facing the adenine sample (top) and the other facing the KCl sample (bottom), which was used for a separate measurement as in the MicroMegas

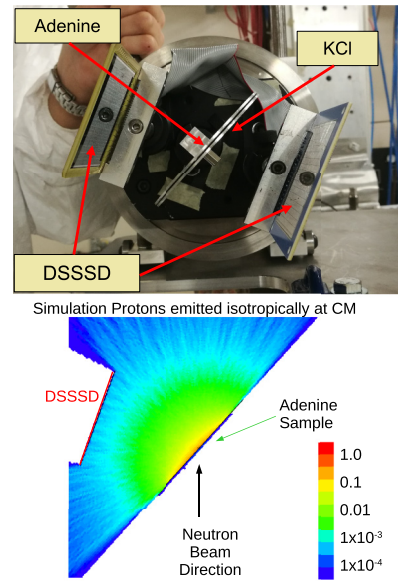

FIG. 2. Top: The DSSSD setup, with the two samples in the center on Al backings (adenine facing upwards and KCl downwards) and two DSSSDs, one facing each sample. Bottom: Simulation to extract the count distribution and detector efficiency considering isotropic proton emission. The position of the adenine sample and the DSSSD are indicated, as well as the incoming neutron beam which serves as the reference direction. The color code corresponds to the proton track density per primary in the simulation.

setup. The center of the detector is at 5.7 cm from the center of the sample. The angular range covered by the strips of the detector is 48°–98°. The beam-spot size at the sample position was 2.14 cm (FWHM). The bottom panel of Fig. 2 shows a simulation of the protons emitted from the sample after the neutron capture reaction. Protons from the (n, p) reaction impinging on the DSSSD deposit all their energy inside the silicon layer. Conversely, those protons emitted from the adenine sample in the backward direction (likewise for the KCl sample) were absorbed by the Al backings. These samples were replaced temporarily at the beginning and end of the measurement with ^{10}B samples for normalization purposes, and also at the end with dummy samples (Al foils) in order to determine the overall background, following the same strategy as with the MicroMegas setup.

The experimental setup was aligned to the nominal beam position. The real position and spatial profile of the beam were checked by the use of Gafchromic foils. These are radiosensitive films that contain a dye that changes color when exposed to ionizing radiation, providing high resolution of the beam profile distribution. The foils were placed at the position of interest. After irradiation, data was processed through digital scanning. This information was also adopted for corrections in the efficiency related to the beam-to-sample intersection.

The detector signals were acquired by the standard n_TOF data acquisition system (DAQ), based on SPDevices ADQ412DC-3G cards of 2 GS/s maximum sampling rate, 12 bits resolution, and 175 MB on-board memory [37]. The special features of these cards ensure the collection of data for

a time of flight (TOF) corresponding to neutron energies well below the thermal energy.

The signal induced by the prompt γ-flash generated in the interaction of the 20 GeV/c proton beam with the lead target was used as a reference signal to determine the time of flight of the neutrons.

C. Samples preparation and characterization

In this measurement, one ^{235}U, one ^{10}B, and two ^{14}N samples were used for the MicroMegas setup. For the DSSSD setup, one ^{10}B and one ^{14}N sample were used. All the sample deposits were 9 cm in diameter in the case of MicroMegas and 5 cm in diameter in the case of DSSSD, which is larger than the neutron beam. The ^{235}U sample, enriched to 99.934%, was prepared with the electrodeposition method and an areal density of 0.1176 ± 0.0005 mg/cm^2 onto 30 μm of Al. The boron samples, with a thickness of 20 nm (MicroMegas) and 25 nm (DSSSD), were made of $^{10}B_4$ C on Al by the sputtering method.

The nitrogen samples were made of adenine ($C_5H_5N_5$) and prepared by thermal evaporation onto Al at CERN. Adenine was used due to a large nitrogen content. At the same time, carbon has a low neutron cross section, and neutron capture on hydrogen produces only γ radiation that is not detected by the MicroMegas detectors. In addition, the proton recoils from elastic scattering of neutrons have lower energy than those from the ^{14}N(n, p) reaction and can be identified and thus filtered out.

The adenine samples were characterized via Rutherford backscattering (RBS) of H^+ at 0.85 MeV at the Centro Nacional de Aceleradores (Spain), where previous works showed excellent possibilities for sample characterization [38]. The RBS spectra were analyzed using the SIMNRA package [39]. In the SIMNRA simulations the Rutherford cross section for the scattering of H^+ in Al was used. For C, N, and H, the evaluated cross section data from the IBANDL database were used [40].

Considering the dimension of the samples (5 and 9 cm in diameter) and of the H^+ beam spot (3 mm) used for the characterization of the samples, several points were analyzed for each sample to provide a picture of the homogeneity of the thickness. The samples were scanned from the edges to the center in three different directions. In order to perform an accurate and precise determination of the number of atoms of ^{14}N, a few points outside the area coated with adenine were also analyzed by RBS. This allowed the determination of any possible contamination of the substrate, reducing the free parameters of the SIMNRA fit of the data. The overall thickness of adenine is revealed both by the presence of the peak and the reduction in energy of the edge from the Al substrate. Figure 3 shows an example SIMNRA fit to the data. The mass density for each measured point was determined with an uncertainty of 1–2%.

We found a smooth reduction of the adenine mass density from the center to the edges. Within uncertainties, the same mass density was found for points at the same distance from the center. Figure 4 reveals a parabolic pattern in the mass density, which was attained through the equation $m = m_0 - ar^2$.

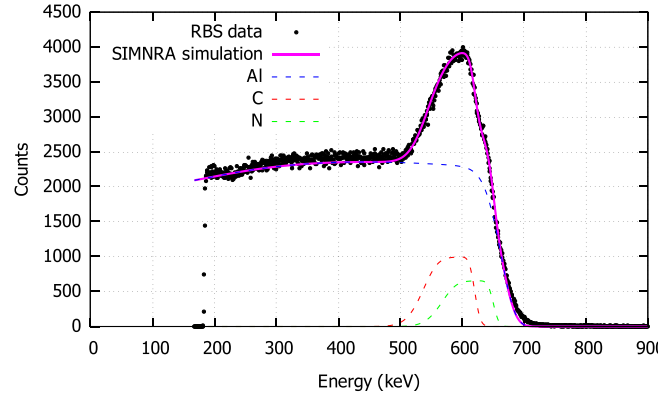

FIG. 3. Example of a single RBS measurement. The results of the SIMNRA fit with detailed contributions from each isotope are also shown with dashed lines.

The parameter a is a measure of the mass distribution throughout the sample, quantified as the curvature of the quadratic fit, while m_0 is the mass density at the center of the samples. The total mass is computed as the integral of the mass density given by the above mentioned formula. The mass of each sample was determined with an uncertainty better than 1.5%. Table I summarizes the results for all the samples.

III. DATA ANALYSIS

The digitized signals from MicroMegas detectors and DSSSD were reconstructed offline by means of a pulse shape analysis routine described in Ref. [41], from which information was extracted on the amplitude, area, timing, and other features of the signals. The analysis was done separately for high intensity (HI) and low intensity (LI) proton pulses from the PS accelerator complex. High intensity pulses (around 7×10^{12} protons per bunch) allow larger statistics, but suffer from a very intense γ flash. On the other hand, low intensity pulses (around 3.5×10^{12} protons per bunch) profit from a reduced γ flash which allows a better signal identification, especially for higher neutron energies. The use of LI pulses

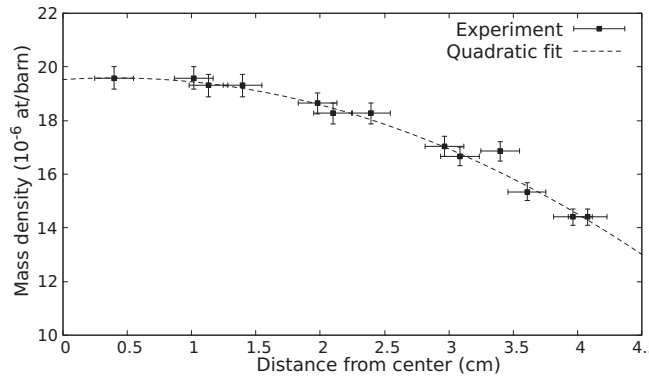

FIG. 4. Mass density radial distribution for the forward adenine sample in the MicroMegas setup. The horizontal error bars match the size of the probe (3 mm). The quadratic fit is shown with a dashed line.

TABLE I. Results of the characterization of the mass density for all the adenine samples.

Sample	m_0 (atoms/b)	a [atoms/(b cm^2)]	Total number of atoms (10^{20} atoms)
DSSSD	6.88×10^{-6}	7.24×10^{-8}	1.306 ± 0.020
Backward MicroMegas	1.382×10^{-5}	2.18×10^{-7}	8.79 ± 0.11
Forward MicroMegas	1.958×10^{-5}	3.91×10^{-7}	9.94 ± 0.12

thus extends the energy range of the measurement in the high energy region, at the expense of a smaller neutron flux and hence lower statistics.

Figure 5 shows a two-dimensional (2D) histogram of the area of the signals versus their TOF for the MicroMegas detector facing the ^{10}B sample, where signals from α particles are discriminated from the other reaction products, electronic noise, and pileup events. The α particles from the two reaction channels—the decay to the ground state (n, α_0) and to the first excited state $(n, \alpha_1\gamma)$—can be observed around 2.0 and 1.7 in area, respectively. Some regions with low number of counts are observed, especially below 10^4 ns, which correspond to dips in the neutron flux caused by Al in the target and beam pipes.

Similarly, a threshold in energy deposition was used to separate the fission fragments from the signals from α decay and electronic noise for the detector facing the ^{235}U sample, as shown in Fig. 6. The figure shows the projection of the signal areas on the vertical axis (of a plot similar to Fig. 5) for several TOF ranges. Individual curves were normalized to prove that the distribution is the same at all energies, hence the correction due to the fraction of fission events lost below the threshold can be considered to be the same at all TOF values.

The residual background within the selection thresholds was measured by means of dummy samples. The relative background at all the neutron energies was found to be well below 10^{-3} for the ^{235}U and ^{10}B samples, therefore it was neglected in the analysis.

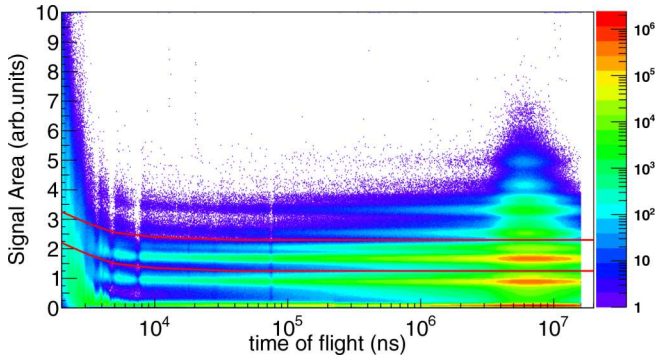

FIG. 5. 2D histogram of deposited energy vs time of flight for the MicroMegas detector in forward emission from ^{10}B. The lines indicate the energy-dependent range applied to select the α particles used in the analysis. The two regions corresponding to the detection of α particles and ^{7}Li are clearly distinguished above and below the bottom red line, respectively. Pileup events can also be observed above the regular signals from α particles. The behavior at low TOF is related to the effect of the γ flash.

In the case of the adenine samples, the emitted proton has a lower energy than the α and ^{7}Li from ^{10}B capture, which makes it more complicated to separate their signals from the low signal area noise and background. Fittings of the count distribution along the whole neutron energy range were performed, in order to estimate the fraction of rejected counts below the selection threshold. Figure 7 shows the counts from the forward adenine sample and the dummy sample used to estimate the background for several neutron energy ranges. The signals from protons between 3.7 and 10 in area can be clearly distinguished above the background. Note an increase of the noise (signals with area lower than about 3) in the detector at higher neutron energies. This noise limits the precision of the background subtraction at neutron energies above 130 keV. Note also the slight increase in energy deposition at higher neutron energies, due to kinematics.

For the analysis of measurement with DSSSD, only coincidence signals from the front and rear strips in the detector were considered in order to reduce part of the background signals appearing at high neutron energies. A time and signal area coincidence rejection was performed. Figure 8 shows a 2D histogram of the signal area versus TOF for the DSSSD facing the adenine sample. The use of only coincident signals has significant impact, especially at TOF corresponding to the first two resonances, where we already see impact of the γ flash. Only signals within a neutron-energy-dependent signal area region, enclosed in red lines in Fig. 8, were considered in the analysis. A small background was subtracted using collected data from dummy samples (Al backings). Nonetheless, there

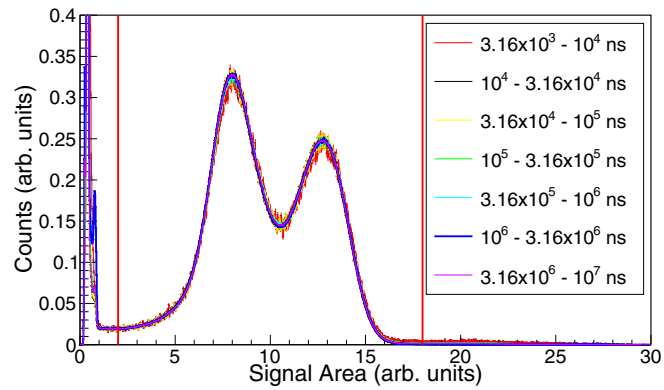

FIG. 6. Energy deposition spectra for seven TOF intervals at the MicroMegas detector facing the ^{235}U sample. The two-bump structure corresponds to the fission fragments' asymmetric masses. The curves were normalized to the same integral between 2 and 18 and indicate that the fraction of fission fragments lost below the threshold is independent of the neutron energy.

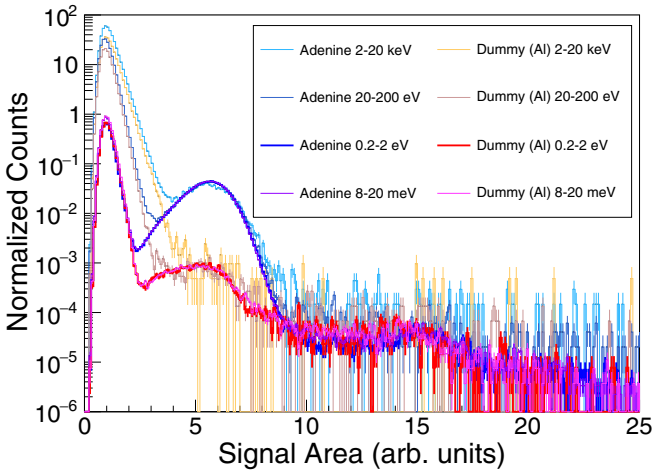

FIG. 7. Energy deposition spectra for four neutron energy intervals in the MicroMegas detector facing the forward adenine sample. The adenine spectra were normalized to the same integral between 3.7 and 10. The background spectra were normalized to the adenine ones using the total proton intensity from the PS pulses.

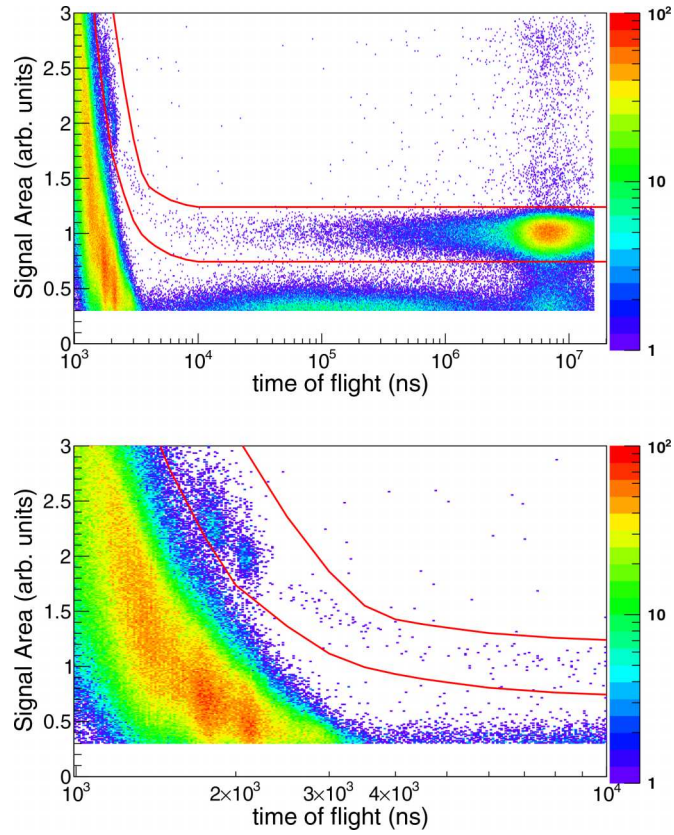

FIG. 8. 2D histogram of deposited energy (signal area) vs TOF for the DSSSD facing the adenine sample. The spectra correspond only to the LI pulses. The red lines indicate the region to select the protons from the ^{14}N(n, p) reaction used in the analysis. Signals below 0.3 in signal area are not shown as they are strongly dominated by the electronic noise. The signals corresponding to the first two resonances can be clearly identified around 2000 ns. The huge number of events at short TOF (lower than 3×10^3 ns) and lower signal area than the protons from the ^{14}N(n, p) reaction are also protons from recoils of elastic scattering of neutrons off hydrogen present in adenine; its structure is related to the EAR-2 spectral flux, which presents several dips in this energy range. These are caused by absorption in Al or Fe present in the target and pipes. The bottom panel is a zoom in the low TOF range.

was an additional small background contribution that cannot be easily subtracted, which was considered in the *R*-matrix (SAMMY) analysis of the data. Pileup events are negligible for all neutron energies due to the low counting rate, given the off-beam location of the DSSSD. A small amount of boron contamination is observed at large TOF from ^{7}Li and α signals. They have higher signal area than the protons (around 1.5 and 2.8 in area in the plot, respectively), and hence do not affect the analysis. As mentioned above, the spectra from LI proton pulses allow analysis up to a higher energy as the background is lower than for the HI ones. Both HI and LI data were used below 300 keV and only LI data were use above that energy, resulting in lower collected statistics in the resonance region.

A. Energy calibration

The TOF-to-energy calibration was performed according to the method described in Ref. [42]. The experimental TOF yield was compared to the simulations from the n_TOF Transport Code, which includes ENDF/B-VIII.0 cross section evaluation with the effect of the n_TOF EAR-2 resolution function. This comparison is shown for the low energy resonances of ^{235}U in Fig. 9. There is an overall good reproduction in the whole range, except in the dips between some of the resonances, which had already been spotted as disagreements between the last ENDF/B-VIII.0 and JEFF-3.3 evaluations. The n_TOF EAR-2 resolution function is dependent on the type of pulses (e.g., by the proton pulse width, 7 ns for HI and 14 ns for LI) and thus the corresponding resolution function data were used in each case. The extracted effective flight path was 19.39 m for the ^{235}U sample position in the MicroMegas chamber. This corresponds to the geometrical distance of the experimental apparatus from the surface of the Pb spallation target. This flight path was adjusted for the subsequent samples according to their position inside the Micromegas chamber. For the DSSSD setup, the flight path was 19.75 m and it was checked by the fitting of the thermal peak and the dips in the flux observed with the reference ^{10}B sample.

B. Neutron fluence and normalization

The ^{14}N(n, p) cross section is extracted relative to the ^{10}B(n, α) cross section according to

$$\sigma_N(E_n) = \sigma_B(E_n)\frac{[C_N(E_n) - B_N(E_n)]\Phi_B(E_n)N_B\epsilon_B}{[C_B(E_n) - B_B(E_n)]\Phi_N(E_n)N_N\epsilon_N}, \quad (1)$$

where C_X ($X \equiv$ N or B for nitrogen and boron, respectively) is the total number of counts in the detector at a given neutron energy E_n and B_X is that of background counts, Φ_X is the neutron fluence, N_X is the areal density of the sample (in atoms per barn), and ϵ_X is the efficiency, which accounts for the geometric efficiency and the event selection thresholds. Reference boron cross-section data were taken from Ref. [43].

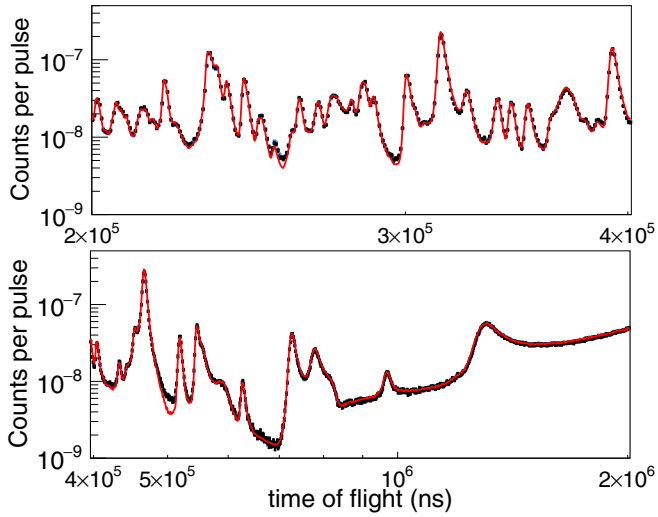

FIG. 9. Measured ^{235}U TOF spectra with MicroMegas in the low energy and resonance region (blue points for LI pulses, black points for HI pulses), compared to the ENDF/B-VIII.0 evaluation (red line) convoluted with the n_TOF EAR-2 resolution function by means of the n_TOF Transport Code. Small differences observed in some valleys are likely from improper values in ENDF/B-VIII.0; compare this database with, e.g., JEFF-3.3.

Along with this, the ^{235}U/^{10}B yield ratio was calculated for validation purposes. A good agreement is found, as shown in Fig. 10, comparing the ratio of the TOF count spectra to the simulations, where the different detection efficiencies and the neutron beam resolution function are considered, following Ref. [42]. The effect of neutron flux attenuation due to the relative positions of the uranium and boron samples was also considered.

C. Efficiency and dead-time corrections

The efficiency corrections for the Micromegas detectors were determined by detailed Monte Carlo simulations of the reaction products' energy loss in the samples and the gas. The simulations were performed with the MCNP6.2 code [44]. In these simulations, we used the actual thickness profiles that

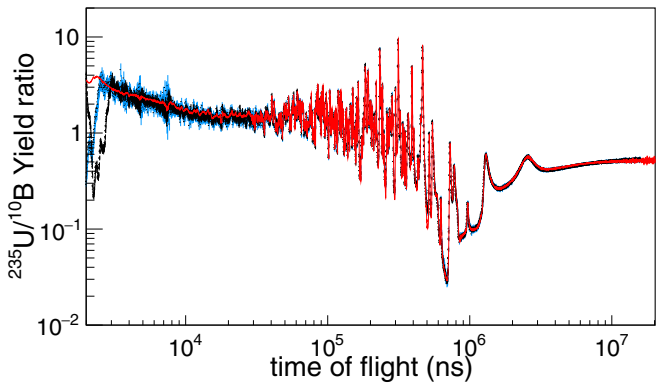

FIG. 10. Measured ^{235}U/^{10}B yield ratio for HI (black) and LI (blue) PS proton pulses, compared to the ENDF/B-VIII.0 evaluation (red) folded with the n_TOF EAR-2 resolution function.

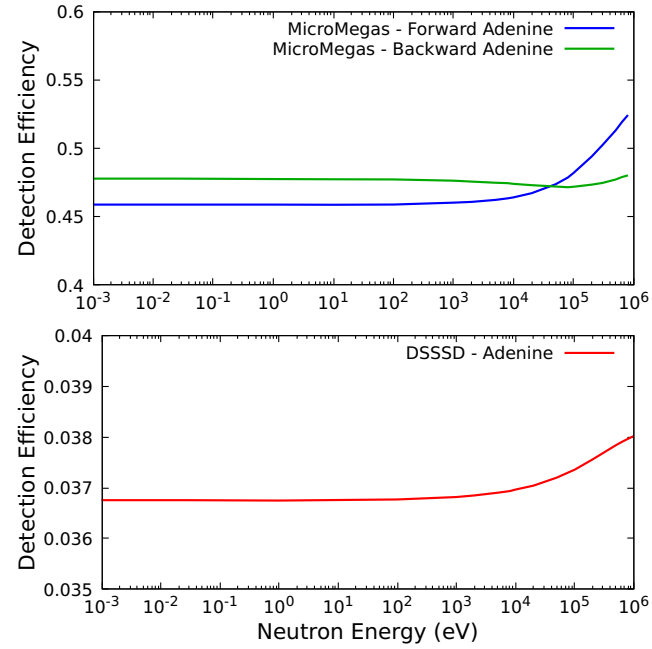

FIG. 11. Upper panel: Simulated detection efficiency of the MicroMegas detectors. Lower panel: Simulated detection efficiency of the DSSSD. Note the different vertical scales for Micromegas and DSSSD.

were found experimentally Energy and angular distributions of emitted charged particles are adopted from [45] for the boron sample, and are assumed to be isotropic at the center of mass for U and for adenine samples at low energy. See Sec. IV B for the check of the distribution from N in the resonance region. The reaction events were assumed to occur uniformly along the beam direction inside the sample, and the beam profile from the n_TOF Transport Code was used. Figure 11 shows the efficiency for the forward and backward adenine samples. As is evident from the figure, the efficiency changes only weakly. The change is seen (due to kinematics) when the incident neutron energy becomes comparable to the reaction Q value. The efficiency at low neutron energy is different for forward and backward samples due to the different thicknesses of the samples (larger for the forward sample), which becomes relevant for proton emission near grazing angles, especially at higher energies. Furthermore, the increasing linear momentum transfer contributes to a larger emission in the forward direction and thus a higher efficiency in the forward case.

For the DSSSD setup, the geometry of the detectors was implemented in the simulations, including the silicon layer thickness and the double strip features, especially regarding the interstrip spacing. The positioning and orientation of the detector with respect to the sample and the beam were checked by using an ^{241}Am source and also the counts from the thermal neutron capture on ^{10}B, assuming isotropic α particle emission. Furthermore, some of the strips from the DSSSD were malfunctioning and were kept out of the analysis. The simulated detection efficiency for the DSSSD adenine sample is shown in the lower panel of Fig. 11.

Dead-time corrections were computed following the non-paralyzable response model [46] assuming a fixed dead time for each detector. The dead times were estimated following two strategies. The first was based on estimating the dead time from the FWHM of the signals and the minimum time difference between consecutive pulses (a sharp cutoff observed in the time-between-pulses distribution). The second method relied on matching the total yield for low and high intensity proton pulses, showing agreement with the first method.

D. Uncertainties

We adopted conservative estimations of the accuracy of the results. The statistical uncertainty of the MicroMegas data was assessed with the use of a binning of 10 bins per decade (bpd), ranging from 0.1% around the thermal point to 4–5% above 10 keV. Statistical uncertainties of the DSSSD data, at 10 bpd, range from 0.4% at thermal energy to 10–15% in the 10–300 keV range. Above 300 keV, the need of a better energy resolution due to the presence of resonances makes us use 100 bpd, at a cost of a higher uncertainty, close to 20% per bin.

The mass of the adenine samples was measured within 1.5% accuracy for the MicroMegas samples. Although the neutron energy dependence of the ^{14}N(n, p) cross section was determined with respect to ^{10}B at all neutron energies [as indicated by Eq. (1)], the absolute cross-section normalization was made using the thermal point of the ^{235}U(n, f) reaction, given that it is a standard at that energy and the U sample mass was known more precisely, with uncertainty of 0.43%, than the B mass. The uncertainty of the cross section of ^{235}U$(n_{\rm th}, f)$ reaction is 0.23% [43].

The uncertainty related to the angular distribution of the α particles from the ^{10}B(n, α) ^{7}Li reaction at higher energies was considered in the calculation of the efficiency in both the MicroMegas and DSSSD setups following the accurate data in Ref. [45]. The uncertainty due to the detection efficiency includes the statistical uncertainty in the simulations of the proton transport (and α particles for the $^{10}B_4$ C sample), which was reduced below 0.2%. Additional uncertainty due to the positioning and orientation of the samples and DSSSD was estimated by simulations with perturbations on the geometry to be 1.3%. The uncertainty in the correction to the selection cuts was estimated to be 1% at thermal energy and up to 5% in the keV range. The effect of the neutron beam attenuation and neutron scattering on Al windows in the n_TOF pipes, Kapton windows of the MicroMegas and DSSSD chambers, the in-beam Micromegas detectors, and upstream samples was assessed via simulations and found to be around 1%. Since DSSSD results are normalized to the MicroMegas data in the $1/v$ region, additional systematic uncertainties from this detection system can be dismissed. The sources of uncertainty are summarized in Table II.

TABLE II. Major sources of uncertainty (in %) of the present ^{14}N(n, p) cross section. The uncertainties vary depending on the binning and the energy range and on the sample.

Component	Uncertainty (%)
Sample mass ^{14}N	1.2–1.5
Normalization	0.65–3
Efficiency and selection cuts	1.8–5
Neutron Beam attenuation	1
Statistical MicroMegas	0.1–5
Statistical DSSSD	0.4–20

IV. RESULTS

A. Data from MicroMegas and DSSSD

The main goal of this measurement was to obtain a consistent data set spanning from thermal to the resonance region and to provide a verification of the first two resonances strengths after a recent paper [1] suggested a possible reduction by a factor of 3.3.

The measurement with MicroMegas detectors covered the range from 8 meV to 80 keV with the backward sample, and up to 130 keV with the forward sample. The extended range for the forward sample is due to its higher mass and slightly higher efficiency at these energies, which leads to an improved signal-to-background ratio. The results from both samples agree with each other within uncertainties. The measurement covers the $1/v$ range, including the thermal point, reproducing and extending the data by Koehler [16]. The high-quality measurement with MicroMegas detectors profits from thick samples and a large detection efficiency.

The measurement with DSSSD detectors then allows extending the range from thermal to 800 keV. This allows full coverage of the astrophysical range of interest, and allows determination of the parameters of the first two observed neutron resonances. The data from DSSSD have a lower counting statistics due to a smaller thickness of the sample and lower geometrical efficiency. The DSSSD data were normalized to that of MicroMegas detectors in the range 8 meV to 100 eV, where there are data from both detection systems.

Overall, this measurement spans eight orders of magnitude of neutron energy, providing for the first time a common consistent dataset for the thermal and $1/v$ range, the astrophysical range, and the resonance region. Figure 12 shows the experimental yield corrected for areal density (Y/N). This quantity differs from the cross section only by the effect of the n_TOF EAR-2 resolution function. Data are presented for both MicroMegas detectors (separately for the forward and backward samples and HI and LI proton pulses) and DSSSD (merged HI and LI below 300 keV, and only LI above 300 keV).

The cross section derived from this yield by means of its fitting with the *R*-matrix based SAMMY code [47] will be shown below. Before that, the angular distribution of the proton emission in the first resonance will be discussed.

B. Angular distribution of protons from the 492.7 keV resonance

Previous measurements of the ^{14}N(n, p) reaction did not carry out any analysis of angular distribution of protons emitted from the resonances. As the DSSSD detects protons emitted only in a range of angles, the knowledge of the angular distribution of emitted protons is crucial for the cross-section determination. In practice, the DSSSD allows one

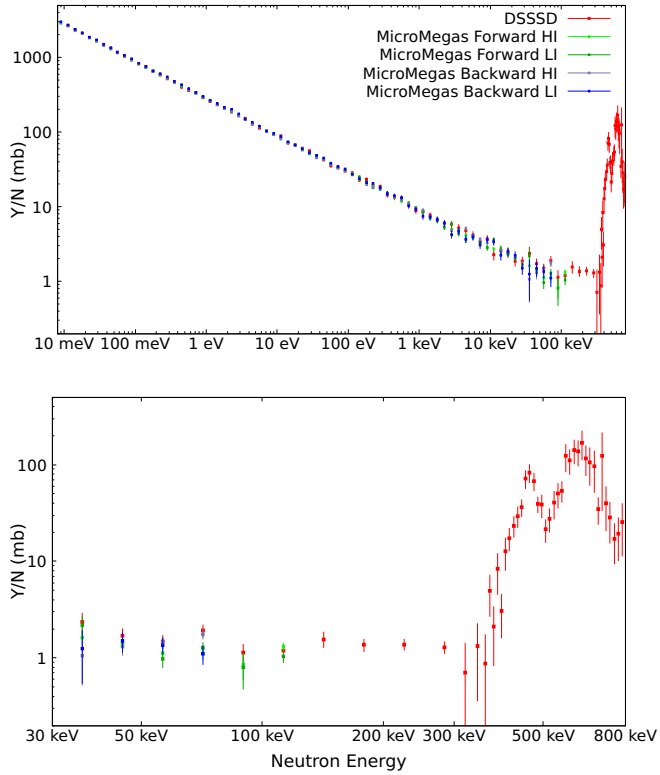

FIG. 12. ^{14}N(n, p) yield/areal density (Y/N) from the experiment. Data are shown at 10 bins per decade below 300 keV and 100 bins per decade above 300 keV. MicroMegas results are separated for forward and backward samples, and also in HI and LI PS proton pulses.

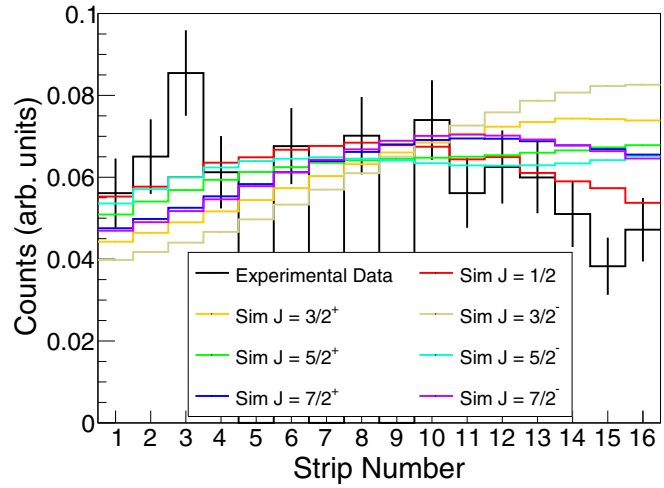

FIG. 13. Experimental counts at the horizontal strips of the DSSSD (black), compared with the simulated distribution of counts for protons emitted isotropically ($J = 1/2$, red) and other resonance spins. The nominal central angle subtended by strip 1 corresponds to an angle of 97.2°and strip 16 corresponds to an angle of 49.5°. Data are normalized so that the total number of counts (from all active strips) is 1. Error bars of the experimental data correspond to statistical uncertainty.

to check the distribution for the first time, even considering its moderate angular resolution. A deviation from isotropy would be an indication that the spin of these resonances is $J > \frac{1}{2}$ and would complicate the determination of the cross section, given the relevance of the angular distribution in the efficiency calculation of the DSSSD setup. The spin and parity for the corresponding ^{15}N state was assigned as $\frac{1}{2}^-$ from a measurement of the ^{14}C(p, γ) reaction [27]. Previous measurements of the inverse reaction ^{14}C$(p, n)^{14}$C then determined the angular distribution of neutron emission, with Sanders [28] observing a possible anisotropy but attributing it to target nonuniformity, and later Gibbons *et al.* not observing any anisotropy at the center of mass [19].

The angular distribution of the protons emitted from the 492.7 keV resonance was analyzed by means of the counts at individual strips in the DSSSD. Dedicated MCNP simulations were run using the proton angular distributions from several J^π resonance options, including $J = 1/2$, where the distribution is isotropic, and also $J^\pi = 3/2^\pm,\ 5/2^\pm,\ 7/2^\pm$, where the angular distribution includes higher-order terms. The computations of the Legendre coefficients were made following Ref. [48] at the center-of-mass reference system and transformed to adapt them to the experimental setup. Resonance widths for this computation were taken from Ref. [30] independently of J^π. Protons were generated along the adenine sample with a spatial distribution given by the neutron beam profile at a distance of 19.75 m from the n_TOF target and the proton energy corresponding to the center of the resonance. Figure 13 shows the count distribution in the strips of the detector in the horizontal direction, that is more sensitive to the angular distribution. The experimental data are in general agreement with a distribution arising from protons emitted isotropically ($J = 1/2$), and deviate clearly from other distributions, especially in strips 1–4 and 11–16. The observed result, compatible with isotropy within uncertainties, is in line with the spin adopted from compilations ($J = \frac{1}{2}$) for the first resonance.

For the determination of the cross section (and resonance parameters) we also need to know the angular distribution from the second resonance at 644 keV. A count distribution compatible with isotropy was also found for the second resonance (though with fewer statistics), also in line with $J = \frac{1}{2}$ from the compilation in Ref. [30].

C. *R*-matrix analysis

To deduce the cross section from the DSSSD yield, data were fitted using the *R*-matrix codeSAMMY [47], applying the Reich-Moore approximation.

In order to illustrate the quality of the SAMMY fit to the yield data, Fig. 14 shows the experimental and fitted yield corrected for the sample areal density. In addition, the deduced cross section (at 300 K) from SAMMY is given. The ENDF/B-VIII.0 evaluation and the Wallner *et al.* results are also shown for comparison. Multiple scattering and self-shielding effects were found to be negligible given the small thickness of the adenine samples. A small constant background was considered in the fit and it was found to be 0.42 ± 0.02 mb. It has no impact on derived resonance parameters and on the cross

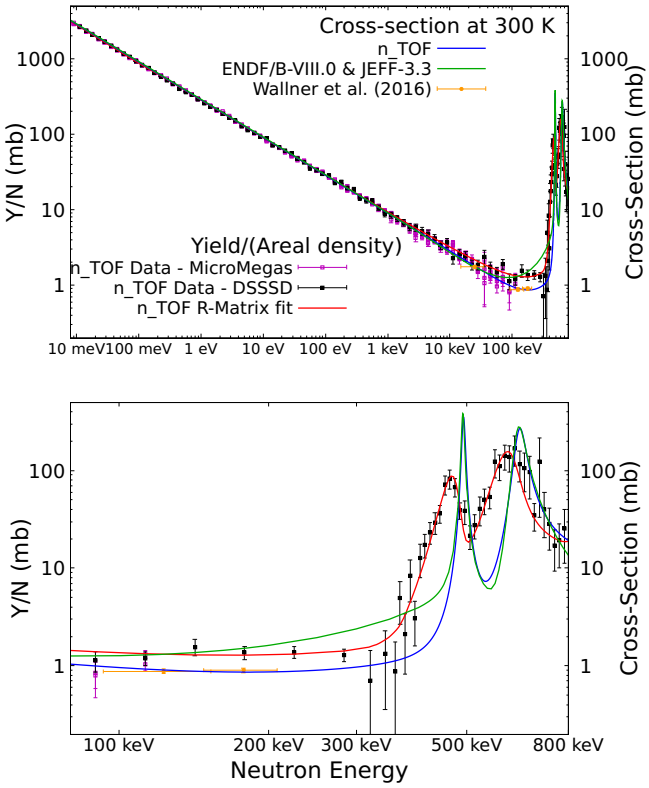

FIG. 14. The yield data corrected for the areal density (Y/N) are shown in black. The red line is the SAMMY fit of the (Y/N) data, the blue line is the cross section at 300 K deduced from parameters obtained with SAMMY. The integral measurements by Wallner *et al.* at 25, 123, and 178 keV are shown in magenta. The ENDF/B-VIII.0 evaluation is included (in green). The upper panel shows the full range covered by this measurement, and the lower panel shows a detail of the resonance region.

section in the $1/v$ region. However, subtracting a constant background becomes relevant at neutron energies between about 50 and 300 keV if we want to reproduce simultaneously the data with the resonance parameters. Furthermore, subtracting this small background is only needed for the DSSSD data, since the MicroMegas yield is fully consistent with no background contribution. We would like to note that the actual background considered in DSSSD data must not necessarily be exactly constant over the whole fitted energies, but must only have a similar value to that required near 100 keV. As the deduced cross section from n_TOF in this region agrees perfectly with Wallner *et al.* data, we have a high confidence that this region is treated correctly.

In the present analysis, the J^π of both resonances was assumed from Ref. [17]. The channel radii were taken as 5.5 fm; Γ_γ, Γ_α, and E_R were fixed to values from Ref. [30], while Γ_n and Γ_p were fitted. The impact of the exact Γ_γ and Γ_α on the fit is negligible provided that they are much smaller than the other widths from Ref. [30]. The 432 keV resonance, reported in Ref. [30] and present in the total cross section of nitrogen [49], was not observed, either in this measurement or in any other papers reporting results at this energy from the ^{14}N(n, p) [24] or the ^{14}C(p, n) reaction [19,50]. Therefore, the Γ_p of this resonance was fixed to zero. Bound states were included in the analysis in order to reproduce the $1/v$ behavior of this reaction below tens of keV. Their positions were again taken from Ref. [30], while Γ_n and Γ_p were adjusted. Other higher-lying resonances (up to 1.5 MeV) were also included in the analysis, fixing all parameters to those in Ref. [30].

The experimental yield was consistently described in the range from 8 meV to 800 keV with the SAMMY fit. The resonance partial widths and resonance strengths—defined as $g\Gamma_n\Gamma_p/\Gamma$, where $\Gamma = \Gamma_n + \Gamma_p + \Gamma_\alpha + \Gamma_\gamma$ is the total resonance width and the statistical factor $g = (2J + 1)/[(2I + 1)(2i + 1)]$, with J, I, and i the spins of the resonant state, the target (1^+) and the projectile $(\frac{1}{2}^+)$, respectively—are listed in Table III.

As mentioned above, the fit of the experimental data includes the effect of the EAR-2 resolution function, which is especially relevant in the resonance region, as clearly seen in the lower panel of Fig. 14. The resolution function broadens the resonances but also shifts the maximum of the resonance in the yield towards lower energy.

The n_TOF cross section describes well the $1/v$ behavior up to 50 keV. In contrast, the ENDF/B-VIII.0 evaluation shows a slight deviation from $1/v$ starting from ≈3 keV. In the resonance region, the n_TOF cross section is consistent within uncertainties with the ENDF/B-VIII.0 evaluation; in terms of the integrated cross section of the resonance, between 450 and 550 keV, the n_TOF reconstructed cross section is 5.1% lower.

A noteworthy situation appears at the low-energy tail of the first resonance (between about 50 and 450 keV), where our cross section differs significantly from the current ENDF/B-VIII.0 evaluation. However, the n_TOF cross section provides a shape much more consistent with the JENDL-5 evaluation in this range. Our shape in this region is also consistent with the data by Johnson *et al.* [24], though only in shape and definitely not in the absolute value of the cross section. Additionally, we are fully consistent with Wallner *et al.* [1] at 127 and 178 keV. The disagreement between ENDF/B-VIII.0 and their cross section led Wallner *et al.* [1] to propose a reduction of the strength of the first resonance by a factor of about 3.3. However, this proposal was based on the assumption that the cross-section energy dependence in ENDF/B-VIII.0 is correct in the region measured by Wallner *et al.*. We thus conclude that the experimental data of Wallner *et al.*, at 127 and 178 keV, as well as those of Johnson *et al.* and Morgan at higher energies, are correct, in disagreement with the ENDF/B-VIII.0 evaluation in the range $E_n \approx$ 3–450 keV.

D. Thermal cross section

The R-matrix fit of the corrected experimental yield (Y/N) allowed also the extraction of the thermal cross section of the ^{14}N(n, p) ^{14}C reaction. It is found to be 1.809 ± 0.045 b. Figure 15 compares this value with results of previous measurements and also with present evaluations. Our result is in agreement with ENDF/B-VIII.0 (JEFF-3.3), while it is lower than the JENDL-5 evaluation, which adopts the original value reported by Wagemans *et al.* [12]. Our result is also compatible within uncertainties in the compilation Atlas of Neutron Resonances by Mughabghab. Compared to the most

TABLE III. Parameters involved in the SAMMY fit of the first two ^{14}N(n, p) ^{14}C resonances. All values without error correspond to fixed parameters in the analysis: J^π was taken from Ref. [17]; Γ_γ, Γ_α, and E_R were fixed using the expectation values from Ref. [30]; $\Gamma_\alpha = 0$ was used in the fitting of the 644 keV resonance; Ref. [30] gives $\Gamma_\alpha < 0.3$ keV. The 432 keV resonance was not observed and thus Γ_p was set to zero. The (n, p) resonance strengths $g\Gamma_n\Gamma_p/\Gamma$ were derived from individual resonance parameters. Uncertainties correspond to the sum of statistical uncertainties (from SAMMY fit) and systematic uncertainties (from normalization of DSSSD data).

E_R (keV)	J^π	Γ_γ (eV)	Γ_α (keV)	Γ_n (keV)	Γ_p (keV)	$g\Gamma_n\Gamma_p/\Gamma$ (keV)
432	$\frac{7}{2}^+$			1.86	0.0	0.0
492.7	$\frac{1}{2}^-$	0.29		1.90 ± 0.15	6.2 ± 0.8	0.48 ± 0.04
644	$\frac{1}{2}^+$	4.2	0.0	35 ± 5	9.2 ± 0.7	2.41 ± 0.22
837	$\frac{1}{2}^+$	19.2	0.0	4.0	400.9	1.32
997	$\frac{3}{2}^+$			43.5	0.8	0.52
1116	$\frac{3}{2}^-$			12.7	4.4	2.18
1184	$\frac{5}{2}^+$			1.3		
1211	$\frac{1}{2}^-$		0.26	14	0.4	0.13
1351	$\frac{5}{2}^+$		0.4	19	0.8	0.75
1405	$\frac{3}{2}^-$		1.8	42	11	5.6

recent and very precise measurement by Kitahara *et al.* [13], our values is lower by about 1.3 standard deviations. We are also in good agreement with the measurements of Gledenov *et al.* [11], as well as with the thermal cross section from the data by Koehler *et al.* [18]. It is lower, but only by about 1.2 standard deviations than results obtained by Wagemans *et al.*, after renormalization of their value due to a change in the ^{235}U$(n_{\rm th}, f)$ cross section used as reference [43]. The same procedure was followed for other previous measurements, for instance for Refs. [11,18], measured relative to ^{6}Li(n, t).

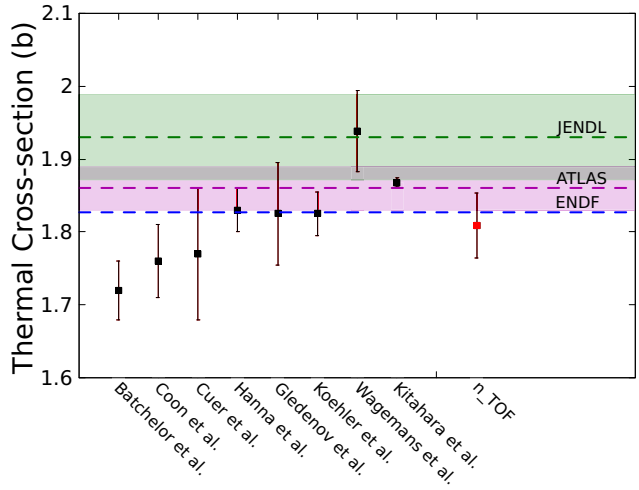

FIG. 15. ^{14}N(n, p) ^{14}C thermal values. Values from ENDF/B-VIII.0 and JEFF-3.3 (blue), JENDL-5 (green), and Atlas of Neutron Resonances (magenta, labeled ATLAS) [30] are indicated with the dashed lines, with semitransparent bands corresponding to uncertainty. Experimental values are marked with squares; our value is shown in red.

E. Maxwellian averaged cross section

Maxwellian averaged cross sections (MACS) were calculated for thermal energies in the range of kT = 5–100 keV, using the cross section obtained from SAMMY. The uncertainties are estimated considering a 2.5% uncertainty in the whole $1/v$ region and the uncertainties in the resonance parameters as given in Table III. The results are listed in Table IV, together with values given by Wallner *et al.* [1] and those derived from the ENDF/B-VIII.0 evaluation cross section. All three MACS agree within uncertainties for kT below about 15 keV. For higher kT the different behavior of the tail of the first resonance results in differences in MACS from different sources. Specifically, the higher cross section considered in ENDF/B-VIII.0 above a neutron energy of about 40 keV makes our MACS smaller. The Wallner *et al.* MACS values

TABLE IV. Maxwellian averaged cross sections derived from the n_TOF cross section, compared with the previous calculation by Wallner *et al.* [1] and the value based on theENDF/B-VIII.0 evaluation cross section [14]. Total uncertainties are given.

kT (keV)	Wallner *et al.*	ENDF/B-VIII.0	n_TOF
5	3.78 ± 0.06	3.81	3.91 ± 0.10
8	3.12 ± 0.05	3.01	3.09 ± 0.08
10	2.89 ± 0.05	2.70	2.76 ± 0.07
15	2.47 ± 0.04	2.26	2.26 ± 0.06
20	2.21 ± 0.04	2.02	1.97 ± 0.05
23	2.09 ± 0.04	1.93	1.84 ± 0.04
25	2.03 ± 0.04	1.88	1.77 ± 0.04
30	1.93 ± 0.04	1.80	1.63 ± 0.04
40	1.85 ± 0.05	1.75	1.47 ± 0.03
50	1.83 ± 0.06	1.86	1.46 ± 0.03
60	1.84 ± 0.07	2.23	1.69 ± 0.04
80	1.84 ± 0.08	3.96	3.14 ± 0.10
100	1.83 ± 0.08	6.92	5.83 ± 0.20

above $kT \approx 60$ keV are strongly impacted by their suggestion related to the strength of the first resonance.

V. SUMMARY AND CONCLUSIONS

A new measurement of the ^{14}N(n, p) ^{14}C reaction was performed at the EAR-2 of the n_TOF facility at CERN. The measurement provides nuclear data from subthermal to the resonance region for the first time, spanning from 8 meV to 800 keV. The cross section is obtained via fitting the experimental yield using the SAMMY code. The obtained thermal cross section is 1.809 ± 0.045 b, in good agreement with ENDF/B-VIII.0 and JEFF-3.3, lower than the JENDL-5 evaluation, and, by slightly more than one standard deviation, lower than values reported from the two most recent dedicated measurements by Wagemans *et al.* [12] and Kitahara *et al.* [13]. Our dependence of the cross section on neutron energy then starts to differ from ENDF/B-VIII.0 and JEFF-3.3 evaluations above about 3 keV. The $1/v$ cross-section dependence is observed for all energies up to about 50 keV and we observe significant disagreement with respect to these evaluations between about 50 and 450 keV, at the low-energy tail of the first resonance at 492.7 keV. On the other hand, our cross section in this range nicely reproduces the cross sections at 25, 123, and 178 keV obtained by Wallner *et al.* [1]. Our resonance integrals of the first two resonances at 492.7 and 644 keV are consistent with the values reported by Morgan and adopted by evaluations. These data could promote new evaluations of the cross section of the ^{14}N(n, p) reaction. With our cross-section data, a calculation of the MACS is carried out and the results show a good agreement with MACS deduced from evaluations at kT below 15 keV, with discrepancies at higher kT.

ACKNOWLEDGMENTS

We thank Mr. Wilhelmus Vollenberg for the preparation of the adenine samples. This work was partially supported by Spanish Ministerio de Ciencia e Innovación (PID2020-117969RB-I00), Junta de Andalucía (FEDER Andalucia 2014-2020) Projects No. P20-00665 and No. B-FQM-156-UGR20. This work was also supported by the UK Science and Facilities Council (ST/M006085/1, ST/P004008/1), by the European Research Council ERC-2015-StG No. 677497, and by the funding agencies of the n_TOF participating institutes. P.T. acknowledges support from the Spanish Ministry of Science, Innovation and Universities under the FPU Grant No. FPU17/02305.

[1] A. Wallner, M. Bichler, K. Buczak, I. Dillmann, F. Käppeler, A. Karakas, C. Lederer, M. Lugaro, K. Mair, A. Mengoni, G. Schätzel, P. Steier, and H. P. Trautvetter, Accelerator mass spectrometry measurements of the ^{13}C(n, γ) ^{14}C and ^{14}N(n, p) ^{14}C cross sections, Phys. Rev. C **93**, 045803 (2016).

[2] C. Abia, K. Cunha, S. Cristallo, and P. de Laverny, The origin of fluorine: abundances in AGB carbon stars revisited, Astron. Astrophys. **581**, A88 (2015).

[3] J. T. Goorley, W. S. Kiger III, and R. G. Zamenhof, Reference dosimetry calculations for neutron capture therapy with comparison of analytical and voxel models, Med. Phys. **29**, 145 (2002).

[4] R. F. Barth, M. H. Vicente, O. K. Harling, W. S. K. III, K. J. Riley, P. J. Binns, F. M. Wagner, M. Suzuki, T. Aihara, I. Kato, and S. Kawabata, Current status of boron neutron capture therapy of high grade gliomas and recurrent head and neck cancer, Radiat. Oncol. **7**, 146 (2012).

[5] International Commission on Radiation Units and Measurements, Photon, electron, proton and neutron interaction data for body tissues, Technical Report No. ICRU-46, Bethesda, MD, 1992, https://www.icru.org/report/photon-electron-proton-and-neutron-interaction-data-for-body-tissues-report-46/.

[6] International Atomic Energy Agency, Advances in Boron Neutron Capture Therapy, Non-serial Publications, IAEA, Vienna (2023), https://www.iaea.org/publications/15339/advances-in-boron-neutron-capture-therapy.

[7] R. Batchelor and B. H. Flowers, Thermal neutron capture in nitrogen, Atomic Energy Research Establishment report, 1949, https://discovery.nationalarchives.gov.uk/details/r/C2964636.

[8] J. H. Coon and R. A. Nobles, Disintegration of ^{3}He and ^{14}N by thermal neutrons, Phys. Rev. **75**, 1358 (1949).

[9] P. Cuer, J.-P. Longchamp, and S. Gorodetzky, Determination of the cross section for reactions of thermal neutrons on nitrogen, J. Phys. (Paris) **12**, 6S (1951).

[10] G. C. Hanna, D. B. Primeau, and P. R. Tunnicliffe, Thermal neutron cross sections and resonance integrals of the reactions ^{17}O$(n, \alpha)^{14}$C, ^{36}Ar$(n, \alpha)^{33}$S, and ^{14}N$(n, p)^{14}$C, Can. J. Phys. **39**, 1784 (1961).

[11] Y. M. Gledenov, V. I. Salatski, and P. V. Sedyshev, The ^{14}N$(n, p)^{14}$C reaction cross section for thermal neutrons, Z. Phys. A **346**, 307 (1993).

[12] J. Wagemans, C. Wagemans, G. Goeminne, and P. Geltenbort, Experimental determination of the ^{14}N (n, p) ^{14}C reaction cross section for thermal neutrons, Phys. Rev. C **61**, 064601 (2000).

[13] R. Kitahara, K. Hirota, S. Ieki, T. Ino, Y. Iwashita, M. Kitaguchi, J. Koga, K. Mishima, A. Morishita, N. Nagakura, H. Oide, H. Otono, Y. Seki, D. Sekiba, T. Shima, H. M. Shimizu, N. Sumi, H. Sumino, K. Taketani, T. Tomita *et al.*, Improved accuracy in the determination of the thermal cross section of ^{14}N(n, p) ^{14}C for neutron lifetime measurement, Prog. Theor. Exp. Phys. **2019**, 093C01 (2019).

[14] M. B. Chadwick, P. G. Young, R. E. MacFarlane, P. Moller, G. M. Hale, R. C. Little, A. J. Koning, and S. Chiba, LA150 Documentation of Cross Sections, Heating, and Damage: Part A (Incident Neutrons) and Part B (Incident Protons), Los Alamos National Laboratory, Technical Report No. LA-UR-99-1222, 1999, http://t2.lanl.gov/publications/la150/la150.html.

[15] S. Druyts, C. Wagemans, and P. Geltenbort, Determination of the ^{35}Cl$(n, p)^{35}$S reaction cross section and its astrophysical implications, Nucl. Phys. A **573**, 291 (1994).

[16] P. E. Koehler and H. A. O'Brien, ^{14}N(n, p) ^{14}C cross section from 61 meV to 34.6 keV and its astrophysical implications, Phys. Rev. C **39**, 1655 (1989).

[17] F. Ajzenberg-Selove, Energy levels of light nuclei $A = 13$–15, Nucl. Phys. A **449**, 1 (1986).

[18] P. E. Koehler, ^{14}N(n, p) ^{14}C cross section near thermal energy, Phys. Rev. C **48**, 439 (1993).

[19] J. H. Gibbons and R. L. Macklin, Total neutron yields from light elements under proton and alpha bombardment, Phys. Rev. **114**, 571 (1959).

[20] K. Brehm, H. W. Becker, C. Rolfs, H. P. Trautvetter, F. Käppeler, and W. Ratynski, The cross section of ^{14}N$(n, p)^{14}$C at stellar energies and its role as a neutron poison for S-process nucleosynthesis, Z. Phys. A **330**, 167 (1988).

[21] Y. M. Gledenov, V. I. Salatski, P. V. Sedyshev, M. V. Sedysheva, V. A. Pshenichnyj, and J. Andrzejewski, Cross sections of the ^{14}N$(n, p)^{14}$C reaction at 24.5, 53.5 and 144 keV, Z. Phys. A **348**, 199 (1994).

[22] T. Sanami, M. Baba, I. Matsuyama, S. Matsuyama, T. Kiyosumi, Y. Nauchi, and N. Hirakawa, Measurement of ^{14}N$(n, p)^{14}$C cross section for $kT = 25.3$ keV Maxwellian neutrons using gridded ionization chamber, Nucl. Instrum. Methods Phys. Res., Sect. A **394**, 368 (1997).

[23] T. Shima, T. Kii, T. Kikuchi, F. Okazaki, T. Kobayashi, T. Baba, Y. Nagai, and M. Igashira, Experimental studies of kev energy neutron-induced reactions relevant to astrophysics and nuclear physics, in *Proceedings of the First Internet Symposium on Nuclear Data, 8–15 April, JAERI, Tokai, Ibaraki, Japan*, JAERI Conference Proceedings No. 97-004, edited by T. Fukahori, O. Iwamoto, and T. Nakagawa (Japan Atomic Energy Research Institute, 1997), p. 131.

[24] C. H. Johnson and H. H. Barschall, Interaction of fast neutrons with nitrogen, Phys. Rev. **80**, 818 (1950).

[25] G. L. Morgan, Cross sections for the ^{14}N(n, p_0), (n, α_0), and (n, α_1) reactions from 0.5 to 15 MeV, Nucl. Sci. Eng. **70**, 163 (1979).

[26] R. J. deBoer, Q. Liu, Y. Chen, M. Couder, J. Görres, E. Lamere, A. Long, S. Lyons, K. Manukyan, L. Morales, D. Robertson, C. Seymour, G. Seymour, E. Stech, B. V. Kolk, and M. Wiescher, Global R-matrix analysis of the ^{11}N(α, n) ^{14}N reaction, J. Phys.: Conf. Ser. **1668**, 012011 (2020).

[27] G. A. Bartholomew, F. Brown, H. E. Gove, A. E. Litherland, and E. B. Paul, Capture radiation and neutrons from the bombardment of C^{14} with protons, Can. J. Phys. **33**, 441 (1955).

[28] R. M. Sanders, Study of the $C^{14}(p, n)N^{14}$ and $C^{14}(\alpha, n)O^{17}$ reactions, Phys. Rev. **104**, 1434 (1956).

[29] M. Niecke, M. Niemeier, R. Weigel, and H. Wirzba-Lorenz, Angular distributions of neutron polarization from the ^{14}C$(p, n)^{14}$N and ^{11}B$(\alpha, n)^{14}$N reactions and R-matrix analysis of ^{15}N in the excitation-energy range between 11.5 and 12.5 MeV, Nucl. Phys. A **289**, 408 (1977).

[30] S. F. Mughabghab, Recommended thermal cross sections, resonance properties, and resonance parameters for $Z = 1$–60, in *Atlas of Neutron Resonances*, 6th ed. (Elsevier, Amsterdam, 2018), pp. 89–822.

[31] E. Chiaveri, O. Aberle, V. Alcayne, S. Amaducci, J. Andrzejewski, L. Audouin, V. Babiano-Suarez, M. Bacak, M. Barbagallo, S. Bennett, E. Berthoumieux, D. Bosnar, A. S. Brown, M. Busso, M. Caamaño, L. Caballero, M. Calviani, F. Calviño, D. Cano-Ott, A. Casanovas *et al.*, Status and perspectives of the neutron time-of-flight facility n_TOF at CERN, EPJ Web Conf. **239**, 17001 (2020).

[32] C. Weiß, E. Chiaveri, S. Girod, V. Vlachoudis, O. Aberle, S. Barros, I. Bergström, E. Berthoumieux, M. Calviani, C. Guerrero, M. Sabaté-Gilarte, A. Tsinganis, J. Andrzejewski, L. Audouin, M. Bacak, J. Balibrea-Correa, M. Barbagallo, V. Bécares, C. Beinrucker, F. Belloni *et al.*, The new vertical neutron beam line at the CERN n_TOF facility design and outlook on the performance, Nucl. Instrum. Methods Phys. Res., Sect. A **799**, 90 (2015).

[33] M. Sabaté-Gilarte, M. Barbagallo, N. Colonna, F. Gunsing, P. Žugec, V. Vlachoudis, Y. H. Chen, A. Stamatopoulos, J. Lerendegui-Marco, M. A. Cortés-Giraldo, A. Villacorta, C. Guerrero, L. Damone, L. Audouin, E. Berthoumieux, L. Cosentino, M. Diakaki, P. Finocchiaro, A. Musumarra, T. Papaevangelou *et al.*, High-accuracy determination of the neutron flux in the new experimental area n_TOF-EAR2 at CERN, Eur. Phys. J. A **53**, 210 (2017).

[34] S. Andriamonje, M. Calviani, Y. Kadi, R. Losito, V. Vlachoudis, E. Berthoumieux, F. Gunsing, A. Giganon, Y. Giomataris, C. Guerrero, R. Sarmento, P. Schillebeeckx, and P. Siegler, A transparent detector for n_TOF neutron beam monitoring, J. Korean Phys. Soc. **59**, 1597 (2011).

[35] J. Praena, M. Sabaté-Gilarte, I. Porras, J. M. Quesada, S. Altstadt, J. Andrzejewski, L. Audouin, V. Bécares, M. Barbagallo, F. Bečvář, F. Belloni, E. Berthoumieux, J. Billowes, V. Boccone, D. Bosnar, M. Brugger, F. Calviño, M. Calviani, D. Cano-Ott, C. Carrapiço *et al.* (n_TOF Collaboration), Measurement and resonance analysis of the ^{33}S$(n, \alpha)^{30}$Si cross section at the CERN n_TOF facility in the energy region from 10 to 300 keV, Phys. Rev. C **97**, 064603 (2018).

[36] Micron Semiconductor Ltd., W1 DC Strip Detectors, http://www.micronsemiconductor.co.uk/product/w1/.

[37] A. Masi, A. A. Paiva, R. Cevenini, E. Chiaveri, M. Donzé, S. Gilardoni, A. Giraud, A. H. Prieto, R. Losito, D. Macina, F. Marazita, P. Peronnard, and L. Tassan-Got, The CERN n_TOF facility data acquisition system, in *Proceedings of the International Conference on Accelerator and Large Experimental Control Systems (ICALEPCS'17), Barcelona, 8–13 October 2017* (JACoW, Geneva, Switzerland, 2018), pp. 1900–1905.

[38] J. Praena, F. Ferrer, W. Vollenberg, M. Sabaté-Gilarte, B. Fernández, J. García-López, I. Porras, J. Quesada, S. Altstadt, J. Andrzejewski, L. Audouin, V. Bécares, M. Barbagallo, F. Bečvář, F. Belloni, E. Berthoumieux, J. Billowes, V. Boccone, D. Bosnar, M. Brugger *et al.*, Preparation and characterization of ^{33}S samples for ^{33}S(n, α) ^{30}Si cross-section measurements at the n_TOF facility at CERN, Nucl. Instrum. Methods Phys. Res., Sect. A **890**, 142 (2018).

[39] M. Mayer, SIMNRA User's Guide, Garching: Max-Planck-Institut für Plasmaphysik, Technical Report No. IPP 9/113, 1997, https://mam.home.ipp.mpg.de/Report%20IPP%209-113.pdf.

[40] IAEA, Ion Beam Analysis Nuclear Data Library (IBANDL), 2014.

[41] P. Žugec, C. Weiß, C. Guerrero, F. Gunsing, V. Vlachoudis, M. Sabate-Gilarte, A. Stamatopoulos, T. Wright, J. Lerendegui-Marco, F. Mingrone, J. Ryan, S. Warren, A. Tsinganis, and M. Barbagallo, Pulse processing routines for neutron time-of-flight data, Nucl. Instrum. Methods Phys. Res., Sect. A **812**, 134 (2016).

[42] V. Vlachoudis, M. Sabaté-Gilarte, V. Alcayne, F. Gunsing, E. Mendoza, F. Ogallar, I. Rejwan, M. Bacak, C. Guerrero, C. Massimi, and A. Stamatopoulos, On the resolution function of the n_TOF facility: A comprehensive study and user guide, CERN Technical Report No. n_TOF-

PUB-2021-001, 2021, https://cds.cern.ch/record/2764434/files/n_TOF-PUB-2021-001.pdf.

[43] A. Carlson, V. Pronyaev, R. Capote, G. Hale, Z.-P. Chen, I. Duran, F.-J. Hambsch, S. Kunieda, W. Mannhart, B. Marcinkevicius, R. Nelson, D. Neudecker, G. Noguere, M. Paris, S. Simakov, P. Schillebeeckx, D. Smith, X. Tao, A. Trkov, A. Wallner *et al.*, Evaluation of the neutron data standards, Nucl. Data Sheets **148**, 143 (2018).

[44] C. J. Werner, J. S. Bull, C. J. Solomon, F. B. Brown, G. W. McKinney, M. E. Rising, D. A. Dixon, R. L. Martz, H. G. Hughes, L. J. Cox, A. J. Zukaitis, J. C. Armstrong, R. A. Forster, and L. Casswell, MCNP Version 6.2 Release Notes, Los Alamos National Laboratory, Technical Report No. LA-UR-18-20808, 2018, https://www.osti.gov/biblio/1419730.

[45] F.-J. Hambsch and I. Ruskov, The $^{10}B(n, \alpha_0)^7$Li and ^{10}B$(n, \alpha_1\gamma)^7$Li alpha-particle angular distributions for $E_n < 1$ MeV, Nucl. Sci. Eng. **163**, 1 (2009).

[46] M. Moore, Rate dependence of counting losses in neutron time-of-flight measurements, Nucl. Instrum. Methods **169**, 245 (1980).

[47] N. M. Larson, Updated users' guide for SAMMY: Multilevel R-Matrix Fits to Neutron Data Using Bayes' Equations, Oak Ridge National Laboratory, Technical Report No. ORNL/TM-9179/R8, 2008, https://info.ornl.gov/sites/publications/files/Pub13056.pdf.

[48] J. M. Blatt and L. C. Biedenharn, The angular distribution of scattering and reaction cross sections, Rev. Mod. Phys. **24**, 258 (1952).

[49] J. J. Hinchey, P. H. Stelson, and W. M. Preston, The total neutron cross section of nitrogen, Phys. Rev. **86**, 483 (1952).

[50] T. R. Wang, R. B. Vogelaar, and R. W. Kavanagh, ^{11}B $+\alpha$ reaction rates and primordial nucleosynthesis, Phys. Rev. C **43**, 883 (1991).